PHYSICAL REVIEW B **106**, 115433 (2022)

Valley selectivity of soft x-ray excitations of core electrons in two-dimensional transition metal dichalcogenides

Andrey Geondzhian
Max Planck Institute for Structure and Dynamics of Matter, 22761 Hamburg, Germany
and Max Planck POSTECH/KOREA Research Initiative, 37673 Pohang, South Korea

Angel Rubio
Max Planck Institute for the Structure and Dynamics of Matter, 22761 Hamburg, Germany
and Center for Computational Quantum Physics (CCQ), The Flatiron Institute,
162 Fifth Avenue, New York, New York 10010, USA

Massimo Altarelli [*]
Max Planck Institute for the Structure and Dynamics of Matter, 22761 Hamburg, Germany

(Received 17 May 2022; revised 4 September 2022; accepted 7 September 2022; published 23 September 2022)

Optical properties of semiconducting monolayer transition metal dichalcogenides have received a lot of attention in recent years, following the discovery of the valley selective optical population of either K_+ or K_- valleys at the direct band gap, depending on the polarization of the incoming light. We use group theoretical selection rules, as well as *ab initio* DFT calculations, to investigate whether this valley selectivity effect is also present in x-ray optical transitions from the flat core level of the transition metal atom to the valence and conduction band K valleys. Valley selectivity is predicted for s, $p_{1/2}$, and $p_{3/2}$ edges in transitions to and from the valence band edges with circularly polarized radiation. Possible novel applications to the diagnostics of valleytronic properties and intervalley dynamics are investigated and the feasibility of ultrafast pump-probe and Kerr rotations experiments with suitable soft-x-ray free-electron laser sources is discussed.

DOI: 10.1103/PhysRevB.106.115433

I. INTRODUCTION

Two-dimensional transition metal dichalcogenides (2D-TMD) provide a very interesting platform for the investigation of two-dimensional solids, with some specific features that differentiate them from either graphene or hexagonal boron nitride (hBN) [1]. In particular, the semiconducting members of this family (MX_2 compounds, with $M =$ Mo, W and $X =$ S, Se, Te) display interesting optical properties in the fundamental gap region; the monolayer gap is direct, and located at two distinct opposite corners of the Brillouin zone, denoted in the following by K_+, K_-, referred to as "valleys," where pronounced exciton effects are observed and where selective optical population of either valley, depending on the sign of the circularly polarized incoming light [2,3], is observed. This effect has led to investigate the potential use of these *"valleytronics"* effects for advanced technological applications. The origin of the effect in 2D-TMD and other compounds with the same symmetry is ascribed to the lack of inversion symmetry and to the mirroring of the K_+, K_- band extrema under time-reversal symmetry [4]. The role of the spin-orbit interaction, frequently emphasized in the literature, however, is not essential (see Appendix A for a numerical example).

One of the hotly discussed topics is the understanding and possible control of the decay time of the difference in occupation of the two valleys, related to the dynamics of electrons, holes and excitons in interaction with the other elementary excitations of the two-dimensional crystal. In this context, it may be of interest to analyze alternative excitation paths, that for example do not simultaneously generate valence band holes and conduction electrons in the selected band valley.

Here we consider the possibility to excite electrons from core levels by absorption of x-ray photons, or to fill core holes by valence electrons in x-ray emission processes, investigating possible valley selectivity effects of the photon polarization. Given that the conduction and valence band valleys have more than 75% metal d-states character [5], it is to be expected that the most intense dipole allowed transitions occur from the p-like core levels of the transition metal atoms, for example, at the $L_{2,3}$, $M_{2,3}$, or $N_{2,3}$ edges, corresponding to $2p$, $3p$, $4p$ core levels (although the low, parity-breaking lattice symmetry allows other possibilities, as we shall soon see).

Very recently, ultrafast far-UV and soft-x-ray spectroscopy investigations of transition metal dichalcogenides films, after

---

[*] massimo.altarelli@mpsd.mpg.de

excitation with a pump laser (with duration <5 fs), have been performed using high harmonic generation sources [6,7], and a free-electron laser [8], with a pump duration ≃50 fs; the samples, however, were multilayer films with several tens of nm thickness, and the photons were not circularly polarized. These pioneering experiments were therefore addressing interesting issues of carrier dynamics, but, because of the sample and photon source properties, were not accessing valleytronic properties, which are the focus of the present work.

Practical reasons suggest to concentrate attention on rather shallow core levels, with ionisation energies restricted to the far UV or soft-x-ray regions. Spectroscopy with photon energies of several keV can only be performed with limited energy resolution, unsuitable to differentiate band features such as primary and secondary valleys; in addition, the photon wave vector at such energies cannot be considered as negligible with respect to the size of the Brillouin zone, and therefore optical transitions cannot be described in the dipole approximation, with initial and final single-electron states with the same quasi momentum in the zone.

This paper is organized as follows. In Sec. II standard group-theoretical techniques are applied to 2D-TMD, recovering the known symmetry characters of valence and conduction band edges [9] but also identifying the irreducible representations of the *s*-, *p*-, and *d*-like core-level edges and deriving the selection rules for optical transitions, for both core and valence excitations. The results, pointing to the valley selectivity of circularly polarized x-ray transitions to the valence bands from the *s* and *p* core-level edges, but not from the *d* edges, are briefly discussed. Transitions into valence band states, of course, require also that the Fermi level is below the valence band top, which can occur by electrostatic gating, by optical pumping or by *p*-type doping. In Sec. III, *ab initio* DFT calculations of the x-ray absorption spectra are presented, that confirm and complement the group theoretical results. In Sec. IV, taking inspiration from existing experimental results for multilayer TMD, we discuss possible contributions of laser pump, soft-x-ray probe spectroscopy to the study of the electronic properties and dynamics of valley-pumped systems. The requirements on the soft-x-ray source (high intensity and monochromaticity, short pulses, and variable polarization) point in the direction of seeded free-electron lasers [10].

II. GROUP-THEORETICAL SELECTION RULES FOR CORE ELECTRON TRANSITIONS

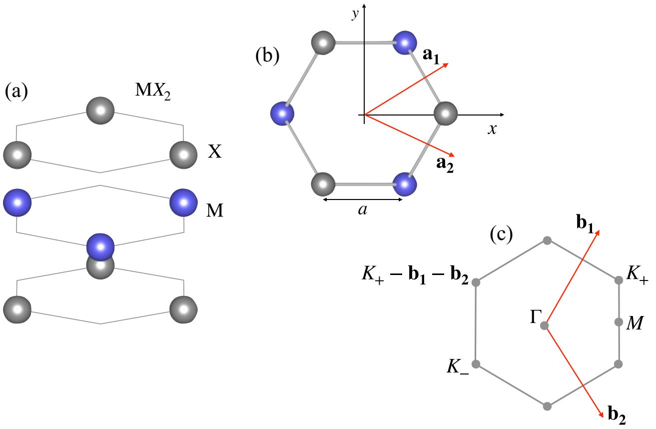

FIG. 1. Structure of MTMDs. Panel (a) shows a perspective side view and panel (b) a top view, including the two unit vectors $\mathbf{a_1}$, $\mathbf{a_2}$ and an orthogonal cartesian frame to describe all vectors in real and reciprocal space. (c) Brillouin zone for the two-dimensional lattice structure, with the unit reciprocal lattice vectors $\mathbf{b_1}$, $\mathbf{b_2}$ and with the two wave vectors of the band structure "valleys," $\mathbf{K}_+$, $\mathbf{K}_-$. A vector equivalent to $\mathbf{K}_+$ is shown for illustration purposes.

Van der Waals multilayer stackings of transition metal dichalcogenides, MX_2, have been investigated for many years. The progress in the manipulation and exfoliation of two-dimensional structures lead more recently to the fabrication of monolayers of the 2H structure that, unlike the multilayer versions, have a direct band gap [1]. In Figs. 1(a) and 1(b) a schematic side and top view of the monolayer structure are shown. It consists of three planes of a triangular arrangement of atoms, with the metal M atoms at the central plane, sandwiched between the two chalcogen X planes, with a stacking that locates metal and chalcogen atoms, when projected on a single plane, at alternating vertices of regular hexagons. If we denote by a the distance of two consecutive vertices of a hexagon [Fig. 1(b)], then a is, e.g., approximately 0.182 nm for MoS$_2$ and 0.189 nm for WSe$_2$, as can be derived from the crystallographic data reproduced by Kormányos *et al.* [11]. In terms of this a length, the cartesian coordinates of the lattice unit vectors $\mathbf{a_1}$, $\mathbf{a_2}$ in terms of the x, y axes of Fig. 1(b) are

$$\mathbf{a_1} = \frac{a}{2}(3, \sqrt{3}), \quad \mathbf{a_2} = \frac{a}{2}(3, -\sqrt{3}). \tag{1}$$

In Fig. 1(c) the corresponding Brillouin zone (BZ) is shown, with the unit vectors of the reciprocal lattice $\mathbf{b_1}$, $\mathbf{b_2}$ and with $\mathbf{K}_+$, $\mathbf{K}_-$ as the two opposite, nonequivalent points where the direct gap is located. It is important to note that, in the same cartesian frame,

$$\mathbf{b_1} = \frac{2\pi}{3a}(1, \sqrt{3}), \quad \mathbf{b_2} = \frac{2\pi}{3a}(1, -\sqrt{3}), \tag{2}$$

and the K_+ and K_- points are not connected by a reciprocal lattice vector,

$$\mathbf{K}_+ = \frac{2\pi}{3a}(1, \sqrt{3}/3) = -\mathbf{K}_-. \tag{3}$$

Also, the star of $\mathbf{K}_+$ only contains (besides itself) $\mathbf{K}_-$ because all other vertices of the hexagonal BZ are connected to either $\mathbf{K}_+$ or $\mathbf{K}_-$ by a reciprocal lattice vector [an example is shown in Fig. 1(c)]. It is important to remember that, since in the case of the 2D-TMD inversion is absent, Kramers' theorem [12] does not apply, and nondegenerate spin bands occur throughout the zone. Furthermore, the point group of the structure shown in Fig. 1 is the dihedral group D_{3h}. To determine the symmetry properties and the selection rules for optical transitions of the Bloch functions at the $\mathbf{K}_+$ or at the $\mathbf{K}_-$ point, we have to consider the "small group" or "wave vector group" at this point, the subgroup of D_{3h} containing the operations that leave this point invariant [13,14]. It easy to see that the C_2 rotations and the corresponding σ_v mirror reflections of D_{3h} interchange the two (nonequivalent) vectors, and are therefore not part of the small group. The remaining operations form the point group C_{3h}. This is a rather simple Abelian group, with six operations and six classes, each comprising one element,

$$E, \quad C_3^+, \quad C_3^-, \quad \sigma_h, \quad S_3^+, \quad S_3^-, \tag{4}$$

where E is the identity, and the $2\pi/3$ rotations C_3 and the rotation-reflections S_3 (about an axis perpendicular to the layer and intersecting the center of a hexagon) are labeled $+$ or $-$, depending on whether they are counterclockwise or clockwise. To obtain all the required information about the representations of the point group C_{3h} and of other groups we shall need later, such as the full rotation-reflection group in three-dimensional space, $O(3)$, many textbooks can be consulted. In the following the notations and conventions of the excellent compilation by Koster, Dimmock, Wheeler, and Statz [15] (KDWS) shall be adopted.

To classify the symmetry of electronic states at the relevant wave vectors $\mathbf{K}_+$ or $\mathbf{K}_-$ we must first determine the action of the six C_{3h} operations on the corresponding Bloch functions. We shall suitably adapt the treatment, as given in Refs. [9,11,16], for the lowest conduction and upmost valence bands to include the case of bands derived from core levels.

A. Symmetry character of conduction and valence levels at $\mathbf{K}_+$, $\mathbf{K}_-$

To establish the basic methods, notations and conventions, we sketch here the derivation of the symmetry properties and optical selection rules for the valence to conduction band transitions (for more details, see Appendix B).

Following the results of *ab initio* and semiempirical band structure calculations, the dominant orbital character of lowest conduction band valleys at $\mathbf{K}_+$ and $\mathbf{K}_-$ is from the $m = 0$ d orbital of the metal atom (with a weight, e.g., for MoS$_2$ estimated [5] at 82%). The remaining fraction is ascribed to p orbitals of the chalcogen, but for symmetry considerations this adds no relevant information. The Bloch function at $\mathbf{K}_\pm$ can be written in the general form [17]

$$\Psi_{c,\mathbf{K}_\pm} = \sum_{j_1,j_2} e^{i\mathbf{K}_\pm\cdot\mathbf{R}_{j_1,j_2}} \Phi_{2,0}\big(\mathbf{r} - \mathbf{R}_{j_1,j_2}\big)\chi(\sigma_z), \tag{5}$$

where (see Fig. 2) the metal atomic sites are identified by the integers j_1, j_2, according to

$$\mathbf{R}_{j_1,j_2} = j_1\mathbf{a_1} + j_2\mathbf{a_2} + \delta_3, \tag{6}$$

having introduced the vectors

$$\delta_1 = \frac{a}{2}(1, \sqrt{3}), \quad \delta_2 = \frac{a}{2}(1, -\sqrt{3}), \quad \delta_3 = a(-1, 0), \tag{7}$$

and having shown in Fig. 2, next to a few atoms, the (j_1, j_2) integer values as examples.

In each term of Eq. (5), the first factor is the Bloch phase factor, $\Psi_{2,0}$ is a Wannier function with $l = 2$, $m = 0$ character and $\chi(\sigma_z)$ denotes the spinor wave function, distinguishing the spin up or down conduction valley. In adopting this form of the Bloch function to discuss the symmetry properties, we implicitly acknowledge that, in the fundamental gap region, the crystal field effects, that lift the fivefold degeneracy of the d orbitals of the metal atoms by several eV's, are more important than the spin orbit interaction, that mixes different m and different σ_z values. To proceed, one must consider the effect of the C_{3h} operations on each factor. In doing so, we follow the standard group-theoretical procedure [13–15] to describe the effect of a space symmetry operation $\hat{C}$ on a generic function f of the space coordinates $\mathbf{r} \equiv (x, y, z)$

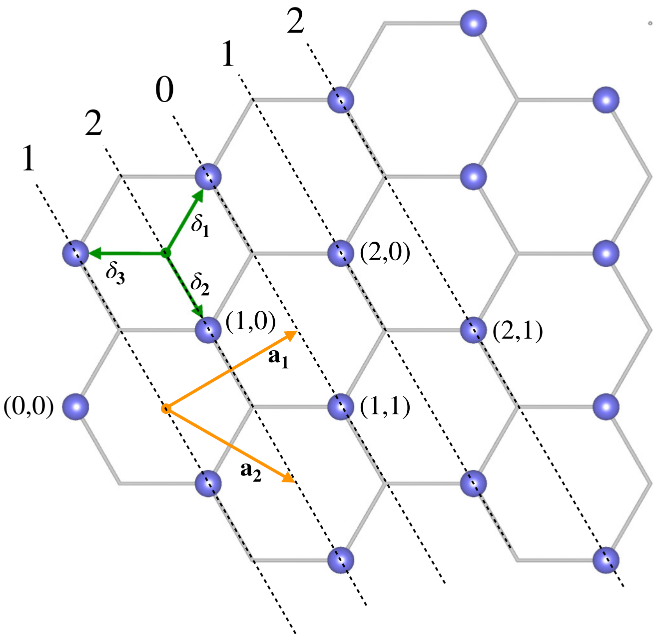

FIG. 2. The middle plane of the monolayer structure, showing the position of the metal atoms and the unit vectors $\mathbf{a_1}, \mathbf{a_2}$. Some atoms are labeled with their j_1, j_2 coordinates as an example. The three vectors δ_i, $i = 1, 2, 3$ are also shown. The dotted diagonal lines are the wavefronts of the $\mathbf{K}_+$ Bloch waves, where $(2j_1 + j_2 - 1)$ is constant (see text). The integers at the top end of the dotted lines are $(2j_1 + j_2 \bmod 3)$.

$$\hat{C}f(\mathbf{r}) = f(\hat{C}^{-1}\mathbf{r}). \tag{8}$$

As detailed in Appendix B, the Bloch phase factor at K$_+$ transforms according to the Γ_3 irreducible representation, and at K$_-$ according to Γ_2; the d-like Wannier function, however, acquires a factor $e^{-im\phi}$ for all rotations about the z axis; so for $m = 0$ it is invariant for all rotations and also for the perpendicular plane reflection, and therefore belongs to Γ_1 [18]. As to the spin wave functions χ, they are by definition a basis for the two-dimensional $D^+_{1/2}$ representation of the full rotation-reflection group O(3), where the $+$ superscript acknowledges that the spin pseudovector is parity even. It is important to recall that when dealing with half-integer spin systems we must consider the "double" groups, resulting from introducing an additional operation $\overline{E}$, that reverses the sign of the half-integer spin functions, but does not affect the space coordinates (equivalently, the additional elements of the group are often described by adding 2π to the angle of every rotation of the group) [13–15]; and consider only the so-called additional representations, odd under $\overline{E}$. When restricted to the operations of C_{3h}, $D^+_{1/2}$ is reducible (the fact that C_{3h} has 6 group elements (12 for the double group) and 6 group classes (12 for the double group) implies that all irreducible representations are one-dimensional, corresponding to the absence of spin degeneracy). We can reduce $D^+_{1/2}$ (as C_{3h} representation) as follows [19]:

$$D^+_{1/2} = \Gamma_7 + \Gamma_8. \tag{9}$$

Therefore, from Ref. [20] at K$_+$:

$$\Gamma_3 \otimes D^+_{1/2} = \Gamma_3 \otimes \Gamma_7 + \Gamma_3 \otimes \Gamma_8 = \Gamma_{10} + \Gamma_{12}. \tag{10}$$

Similarly, at K$_-$:

$$\Gamma_2 \otimes D^+_{1/2} = \Gamma_2 \otimes \Gamma_7 + \Gamma_2 \otimes \Gamma_8 = \Gamma_{11} + \Gamma_9, \tag{11}$$

with the two representations corresponding to the two spin directions.

Note that $\Gamma_{9,11}$ are respective complex conjugates of the $\Gamma_{10,12}$. This is a reformulation of the time reversal symmetry condition $E_n(\mathbf{k}, \uparrow) = E_n(-\mathbf{k}, \downarrow)$ implied by the discussion immediately following Eq. (3).

Consider now the top of the valence bands. The corresponding dominant orbital is the metal d orbital with $m = \pm 2$ [17], schematically behaving as $(x \pm iy)^2$. We can write the Bloch functions as

$$\Psi_{v,\mathbf{K}_\pm} = \sum_{j_1,j_2} e^{i\mathbf{K}_\pm\cdot\mathbf{R}_{j_1,j_2}}\,\Phi_{2,\pm2}\big(\mathbf{r} - \mathbf{R}_{j_1,j_2}\big)\chi(\sigma_z). \tag{12}$$

In either case, namely, K$_+$, $m = +2$ or K$_-$, $m = -2$ it is readily seen that the product of the Bloch factor and the d-like Wannier function is invariant under all C_{3h} operations [2], belonging to the Γ_1 identical representation. The overall Bloch function with the spin part is a basis for the $D^+_{1/2}$, and we already know that $D^+_{1/2} = \Gamma_7 + \Gamma_8$.

On the basis of this symmetry assignment, it is possible to establish the selection rules for optical transitions. The group theoretical necessary but not sufficient prescription for a nonvanishing transition matrix element from an initial state ψ_i to a final state ψ_f under the transition operator ($\hat{T}^\alpha$),

$$\hat{T}^\alpha_{i,f} = \langle\psi_i|\hat{T}^\alpha|\psi_f\rangle = \int d^3r\,\psi^*_i(\mathbf{r})\hat{T}^\alpha\psi_f(\mathbf{r}), \tag{13}$$

can be expressed as [21]

$$\Gamma_\alpha \otimes \Gamma_f = \Gamma_i. \tag{14}$$

The fact that the "small" group of the wave vectors $\mathbf{K}_+$, $\mathbf{K}_-$ has only one-dimensional irreducible representations makes our life much easier (do not need to specify and discuss individual rows of irreducible representations). For the valence and conduction edges we determined the representations; for the transition operator $\mathbf{A}\cdot\mathbf{p}$, corresponding to dipole optical transitions, we have the vector potential

$$\mathbf{A}\cdot\mathbf{p} \sim \sum_{\mathbf{k},\lambda}[\epsilon_\lambda b_{\mathbf{k},\lambda}e^{i\mathbf{k}\cdot\mathbf{r}} + \epsilon^*{}_\lambda b^+_{\mathbf{k},\lambda}e^{-i\mathbf{k}\cdot\mathbf{r}}]\cdot\mathbf{p}, \tag{15}$$

where ϵ denotes the polarization vector of mode $\lambda = \pm 1, 0$ for positive circular, negative circular and linear z polarization, respectively, and b^+, b are photon creation and annihilation operators. Including also the photon states, we can precisely define the transition operator in Eq. (15) for a photon absorption process as

$$\begin{aligned}&\langle\psi_i; n_\lambda|\hat{T}^\alpha|\psi_f; n_\lambda - 1\rangle\\ &\quad = \langle\psi_i; n_\lambda|[\epsilon^*{}_\lambda b^+_{\mathbf{k},\lambda}e^{-i\mathbf{k}\cdot\mathbf{r}}]\cdot\mathbf{p}|\psi_f; n_\lambda - 1\rangle,\end{aligned} \tag{16}$$

with $n_\lambda, n_\lambda - 1$ denoting the number of photons of the λ polarization in the initial and final state, respectively.

The transition operator (in the $\mathbf{k} \longrightarrow 0$ limit) contains therefore $\epsilon_\lambda \cdot \mathbf{p}$ (for photon emission) and $\epsilon^*{}_\lambda \cdot \mathbf{p}$ (for photon absorption), therefore transforms like the components of the $\mathbf{p}$ vector, i.e., like the $l = 1$ spherical harmonics, or the D^-_1 representation of $O(3)$. The reduction of D^-_1 in C_{3h} is [22]

$$D^-_1 = \Gamma_2 + \Gamma_3 + \Gamma_4 \tag{17}$$

and from a look at the character table of C_{3h}, keeping in mind the convention embodied in Eq. (8) and applying it to $l = 1$ spherical harmonics [23], it is easy to establish that

$$\begin{aligned}\epsilon_{+1}, \epsilon^*_{-1} &\sim (p_x + ip_y) \longrightarrow \Gamma_3,\\ \epsilon_{-1}, \epsilon^*_{+1} &\sim (p_x - ip_y) \longrightarrow \Gamma_2,\\ \epsilon_0 &\sim p_z \longrightarrow \Gamma_4,\end{aligned} \tag{18}$$

thus assigning the proper symmetry to positive and negative circular polarization for propagation perpendicular to the plane, and to linear polarization perpendicular to the plane. We are especially concerned with the first two, that determine the chirality of optical properties of MTMD. Taking Eq. (16) into account, we identify Γ_2, ($\hat{T}^\alpha \sim \epsilon^*_{+1}$) as the "+" circular polarization, and Γ_3 ($\hat{T}^\alpha \sim \epsilon^*_{-1}$) as the "−" one, following the convention implicitly assumed in Ref. [2].

A straightforward perusal of the C_{3h} table of multiplication [22] and character table [24], yields the following allowed transitions from the valence band state Γ_7, Γ_8, for circularly polarized positive (+) or negative (−) photons.

At $\mathbf{K}_+$:

Initial	Final	Polarization
Γ_7	Γ_{10}	+
Γ_8	Γ_{12}	+

At $\mathbf{K}_-$:

Initial	Final	Polarization
Γ_7	Γ_{11}	−
Γ_8	Γ_9	−

[It may appear surprising that photons with angular momentum ±1 may connect states labeled with $m = 0$ with states $m = \pm 2$. This occurs because the symmetry of the crystal breaks full rotation invariance around the z axis (normal to the plane). Only rotations multiples of $2\pi/3$ survive. For such restricted set of rotations, the values of m are to be understood as m mod 3, so that $m = 2$ mixes with $m = -1$, $m = -2$ with $m = 1$, etc.]

This recovers the remarkable effect of the valley selectivity for circularly polarized photons. It is important to observe that although the excitonic character of the observed optical transitions at the fundamental gap is very pronounced [1], this does not alter the selection rules derived from one-electron Bloch functions at the relevant edges, as the excitonic wave function satisfies those symmetries.

B. Symmetry character of core levels at K$_+$, K$_-$

As already mentioned in the Introduction, the core electron levels have very distinctive features when compared to valence states: one is their very localized character, so that, when described in terms of bands in momentum space, they have negligible dispersion and very large effective masses. In addition, the spin-orbit splitting of core levels (except the s-like ones) is much larger than for valence states and constitutes an energy scale exceeding the fundamental band gap and in most cases the typical bandwidth of valence levels (see a compilation of atomic binding energies of Mo and W in Appendix E). Before dealing with the discussion of strongly spin-orbit-split p and d core levels, let us briefly address the s-like core levels. This can in point of fact proceed very quickly, as the discussion parallels completely that of the conduction band bottom. From the point of view of the C_{3h} group, the conduction band Wannier function $\Phi_{2,0}$ and the s-like function $\Phi_{0,0}$ have exactly the same symmetry properties of invariance under all group operations. Therefore, we obtain the symmetry classification of Γ_{10}, Γ_{12} for the two spin orientations at $\mathbf{K}_+$ and Γ_9, Γ_{11} at $\mathbf{K}_-$. This is enough to conclude that, in p-type samples, transitions to the valence band top shall display the valley selectivity of polarized photons. Transitions to the conduction band minima, corresponding to states with symmetry identical to the s core levels, are forbidden.

Going back to the strongly spin-orbit split p and d levels, it appears appropriate to modify the description of Bloch functions as given in Eqs. (5) or (12) by diagonalizing at the very start the spin-orbit interactions and replacing the eigenfunctions of l, m, and σ_z with those of j and j_z. Given the very nearly dispersionless nature of the core bands, all the $2j+1$ values of j_z are degenerate, to a very good approximation, throughout the Brillouin zone and constitute a basis for the $D_j^{\pm}$ representation of $O(3)$; the $\pm$ sign ambiguity depends on the parity of the spatial wave functions, e.g., odd for $p_{1/2}$ or $p_{3/2}$ levels, even for $d_{3/2}$ or $d_{5/2}$, etc.

Thus, the general form of a core wave function is

$$\Psi_{n,l,j,j_z\mathbf{K}_\pm} = \sum_{j_1,j_2} e^{i\mathbf{K}_\pm\cdot\mathbf{R}_{j_1,j_2}}\Phi_{n,l,j,j_z}\big(\mathbf{r}-\mathbf{R}_{j_1,j_2}\big). \tag{19}$$

From the discussion of the valence levels, we learned that the Bloch factor in each addendum transforms like Γ_3 for $\mathbf{K}_+$ and like Γ_2 for $\mathbf{K}_-$. Therefore, the complete Bloch function transforms like the product representation

$$\mathbf{K}_+: \quad \Gamma_3\otimes D_j^{\pm}, \qquad \mathbf{K}_-: \quad \Gamma_2\otimes D_j^{\pm}, \tag{20}$$

with the *odd* D_j^- representation for p core levels, and the *even* D_j^+ for the d-like levels.

From tabulated results [22] we have the following reductions:

$$D_{1/2}^- = \Gamma_9 + \Gamma_{10}, \tag{21}$$

$$D_{3/2}^- = \Gamma_9 + \Gamma_{10} + \Gamma_{11} + \Gamma_{12}, \tag{22}$$

which allow us to identify the reduction of the complete Bloch functions for $p_{1/2}$ and $p_{3/2}$ functions, i.e., for $L_2, L_3, M_2, M_3, N_2, N_3$,... core levels. Starting with the $p_{1/2}$ levels at the $\mathbf{K}_+$ point, from Eq. (21) they belong to the following representations:

$$\Gamma_3\otimes\Gamma_9 = \Gamma_8; \quad \Gamma_3\otimes\Gamma_{10} = \Gamma_{11}, \tag{23}$$

and at the $\mathbf{K}_-$ point, to the representations

$$\Gamma_2\otimes\Gamma_9 = \Gamma_{12}; \quad \Gamma_2\otimes\Gamma_{10} = \Gamma_7. \tag{24}$$

We are then in a position to derive the selection rules for optical transitions to the conduction band minima, using again Eqs. (13)–(16). The only allowed transitions are
at $\mathbf{K}_+$:

Initial	Final	Polarization
Γ_8	Γ_{12}	+
Γ_{11}	Γ_{10}	−

at $\mathbf{K}_-$:

Initial	Final	Polarization
Γ_{12}	Γ_9	+
Γ_7	Γ_{11}	−

We therefore conclude that the valley selectivity effect for dipole transitions to the conduction band edges *does not occur* at the $p_{1/2}$-like absorption edges L_2, M_2, N_2. This includes the cases of intrinsic or n-type samples, where the Fermi level is in the gap or in the conduction bands. For samples, where empty states near the top of the valence bands (i.e., in the Γ_7 and/or Γ_8 bands) occur, however, the selection rules for transitions from the $p_{1/2}$ core levels are
at $\mathbf{K}_+$:

Initial	Final	Polarization
Γ_{11}	Γ_7	+

at $\mathbf{K}_-$:

Initial	Final	Polarization
Γ_{12}	Γ_8	−

In this case of p-type samples, therefore, the valley selectivity should be in principle observable at the L_2, M_2, N_2 absorption edges. Also, x-ray emission deriving from transitions from the full valence band states to core holes should obey related selection rules (interchanging initial and final states and the sign of the polarization).

We now consider the $p_{3/2}$ levels. From Eq. (22) one obtains that, at the $\mathbf{K}_+$ point they correspond to the following representations:

$$\begin{aligned}&\Gamma_3\otimes\Gamma_9 = \Gamma_8; \quad \Gamma_3\otimes\Gamma_{10} = \Gamma_{11};\\ &\Gamma_3\otimes\Gamma_{11} = \Gamma_7; \quad \Gamma_3\otimes\Gamma_{12} = \Gamma_9,\end{aligned} \tag{25}$$

and at $\mathbf{K}_-$:

$$\begin{aligned}&\Gamma_2\otimes\Gamma_9 = \Gamma_{12}; \quad \Gamma_2\otimes\Gamma_{10} = \Gamma_7;\\ &\Gamma_2\otimes\Gamma_{11} = \Gamma_{10}; \quad \Gamma_2\otimes\Gamma_{12} = \Gamma_8.\end{aligned} \tag{26}$$

Notice that Γ_7 and Γ_8 levels are present at both points, and we know from the discussion of the valence band transitions that these symmetries imply the valley selectivity of optical absorption to the conduction bands. It remains to investigate which transitions are allowed from the Γ_9 and Γ_{11} levels to the Γ_{10} and Γ_{12} levels at $\mathbf{K}_+$, and from the Γ_{10} and Γ_{12} levels Γ_9 and Γ_{11} levels at $\mathbf{K}_-$. The analysis based on Eq. (14) gives the following results for allowed transitions
at $\mathbf{K}_+$:

Initial	Final	Polarization
Γ_7	Γ_{10}	+
Γ_8	Γ_{12}	+
Γ_9	Γ_{12}	−
Γ_{11}	Γ_{10}	−

at $\mathbf{K}_-$:

Initial	Final	Polarization
Γ_7	Γ_{11}	$-$
Γ_8	Γ_9	$-$
Γ_{10}	Γ_{11}	$+$
Γ_{12}	Γ_9	$+$

Therefore, both valleys are accessible with both polarizations, and no valley selectivity holds for transitions to the conduction bands. Once again, considering *p*-type samples (or x-ray emission spectroscopy), we obtain, however, for Γ_7, Γ_8 final states

at $\mathbf{K}_+$:

Initial	Final	Polarization
Γ_{11}	Γ_7	$+$
Γ_9	Γ_8	$+$

at $\mathbf{K}_-$:

Initial	Final	Polarization
Γ_{10}	Γ_7	$-$
Γ_{12}	Γ_8	$-$

Therefore, one can expect valley selective absorption in *p*-type samples, or emission from valence band states to core holes at L_3, M_3, and N_3 edges.

Finally, let us now turn our attention to the *d*-like core levels, that are split into $d_{3/2}$ and $d_{5/2}$, respectively corresponding to the representations $D^+_{3/2}$, $D^+_{5/2}$. From Ref. [22] the reduction to irreducible C_{3h} representation gives

$$D^+_{3/2} = \Gamma_7 + \Gamma_8 + \Gamma_{11} + \Gamma_{12}, \tag{27}$$

$$D^+_{5/2} = \Gamma_7 + \Gamma_8 + \Gamma_9 + \Gamma_{10} + \Gamma_{11} + \Gamma_{12}. \tag{28}$$

We thus see that the sixfold degenerate $d_{5/2}$ state contains *all* six additional irreducible representations of C_{3h}. They shall also all appear both at $\mathbf{K}_+$ ($\mathbf{K}_-$), because multiplication by Γ_2 (Γ_3) of the whole list of representations shall deliver a permutation of the same list. This tells us without further calculations that the valley selectivity *does not occur* at $d_{5/2}$ edges, where all possible symmetries and transitions occur at both $\mathbf{K}_\pm$ points. An explicit calculation shows that the selectivity is lost also at the $d_{3/2}$ edges. In fact, the fourfold degeneracy of this state is split into four representations, namely, at $\mathbf{K}_+$:

$$\Gamma_3 \otimes \Gamma_7 = \Gamma_{10}; \quad \Gamma_3 \otimes \Gamma_8 = \Gamma_{12};$$
$$\Gamma_3 \otimes \Gamma_{11} = \Gamma_7; \quad \Gamma_3 \otimes \Gamma_{12} = \Gamma_9 \tag{29}$$

and at $\mathbf{K}_-$:

$$\Gamma_2 \otimes \Gamma_7 = \Gamma_{11}; \quad \Gamma_2 \otimes \Gamma_8 = \Gamma_9;$$
$$\Gamma_2 \otimes \Gamma_{11} = \Gamma_{10}; \quad \Gamma_2 \otimes \Gamma_{12} = \Gamma_8. \tag{30}$$

This combination of symmetries is not verifying valley selectivity. For example, we find at $\mathbf{K}_+$:

Initial	Final	Polarization
Γ_9	Γ_{12}	$-$
Γ_7	Γ_{10}	$+$

and similarly at $\mathbf{K}_-$:

Initial	Final	Polarization
Γ_{10}	Γ_{11}	$+$
Γ_8	Γ_9	$-$

so that transitions with both polarizations are allowed in both valleys. It is also easily verified that no selectivity is present in *p*-type samples either. In the following section we will use first-principle calculations to confirm all the selection rules obtained for high symmetry points, and extend them through large regions of the Brillouin zone.

III. NUMERICAL CALCULATIONS OF TRANSITION RATES

To confirm the findings of the group-theoretical analysis of the selection rules for the $\mathbf{K}_+$ and $\mathbf{K}_-$ band edges, DFT *ab initio* calculations were performed throughout the Brillouin zone for the prototypical MoS_2 MTMD, using the all-electron *exciting* code [25] with linearized augmented plane-wave and local orbitals (LAPW + lo) basis set [26]. In this way, the rapid oscillation of the localized wave functions around the nuclear position is handled in the local atomic orbital basis within the sphere of the "muffin-tin" radii and the rest of the solid (interstitial region) in the plane-wave basis. Due to the dominance of the relativistic effects for the core states, we obtained core-state wave functions by solving the set of coupled Dirac equations in a spherically symmetric potential as implemented in *exciting* [25,28]. In contrast, the conduction and valence states were obtained in the scalar-relativistic approximation. The latter also implies that the small components of the four-spinor wave function were neglected when calculating the transition matrix elements. We employ the generalized gradient approximation (GGA) PBE [27] for exchange-correlation functional, a momentum space grid of 21 × 21 × 1 points, and a muffin-tin radius of 2 a.u. for both species. Excitonic effects were not included at this stage, as they should not alter the main results and conclusions, for the reasons outlined later, at point 2 in Sec. V.

The selected core level is the Mo $3p_{3/2}$, or M_3 level, which (see Table I) is located about 390 eV below the Fermi energy. The quantity that is computed and plotted is the normalized "degree of optical polarization" η as defined in Ref. [2], for the transitions from the four degenerate $p_{3/2}$ levels to the band *b*,

$$\eta_{p_{3/2}-b}(\mathbf{k}) = \sum_{j=-3/2}^{3/2} \frac{|D_+^{jb}(\mathbf{k})|^2 - |D_-^{jb}(\mathbf{k})|^2}{|D_+^{jb}(\mathbf{k})|^2 + |D_-^{jb}(\mathbf{k})|^2}, \tag{31}$$

where

$$D_\pm^{jb}(\mathbf{k}) = \left[D_x^{jb}(\mathbf{k}) \pm i D_y^{jb}(\mathbf{k})\right], \tag{32}$$

and *D* is the appropriate component of the momentum matrix element from the core level *j* to the valence or conduction band edge *b*. The results for transitions to the valence and to the conduction band are shown in Figs. 3 and 4, respectively. Furthermore, to show the energy dependence of the corresponding transition, we calculated the absorption spectra (σ)

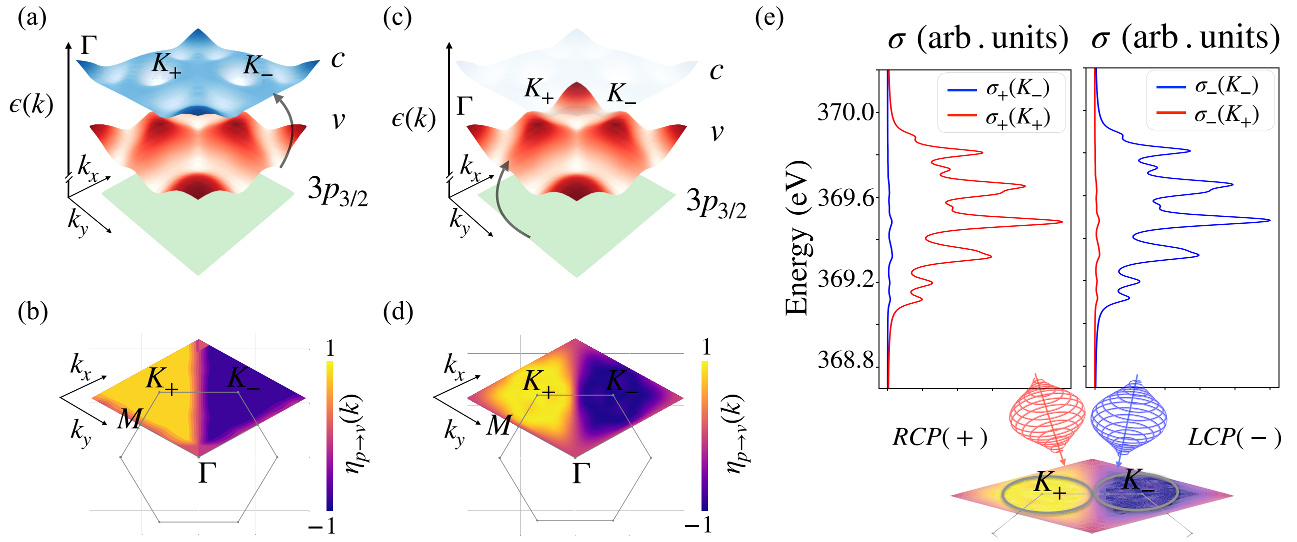

FIG. 3. Valley selectivity for transitions from the Mo fourfold degenerate $3p_{3/2}$ level to the uppermost valence bands. (a), (c) Sketches of the valence to conduction band transition (a) and the core to valence band transition (c); (b), (d) Computed normalized degree of optical polarization η (see text) as a function of quasi-momentum $\mathbf{k}$ in the relevant portion of the Brillouin zone for the valence to conduction and core to valence band transitions, respectively; (e) Partial absorption cross-section (σ) obtained through integration over a circular area around $\mathrm{K}_\pm$ points for left (−) and right (+) circular polarization of the incoming x-ray photons [see also text and illustration of the absorption process in the bottom of panel (e)].

in the independent particle limit in vicinity of $\mathrm{K}_\pm$ points,

$$\sigma_\pm(\omega) = \sum_{j,b}\int_{\Omega(k_{\max})} d\mathbf{k}|D_\pm^{jb}(\mathbf{k})|^2\delta[\omega - E_b(\mathbf{k}) - E_j(\mathbf{k})]. \tag{33}$$

Here the integration area $\Omega(k_{\max})$ is defined by the parameter $k_{\max}$ as $|\mathbf{k}-\mathbf{K}_\pm| < k_{\max}$. The latter is chosen to be the half of the distance between the $\mathbf{K}_+$ and $\mathbf{K}_-$ points. The transition matrix elements $M_{jb}(\mathbf{k})$ between core and valence (conduction) states were calculated in the dipole approximation and E_j, E_b are the energies of the corresponding levels. A small Lorentzian broadening was attributed to the resulting spectra for visual purposes. Such partial absorption cross-sections are equal for left and right circular polarization of the incoming photon if there is no valley selectivity at a given energy

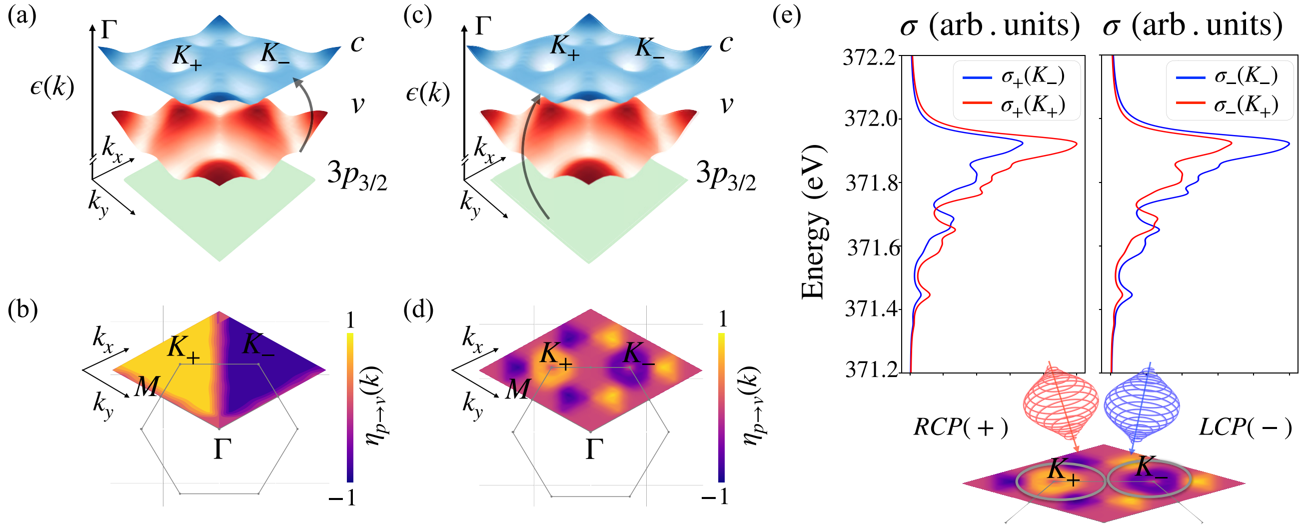

FIG. 4. Valley selectivity for transitions from the Mo fourfold degenerate $3p_{3/2}$ level to the lowest conduction band. (a), (c) Sketches of the valence to conduction band transition (a) and the core to conduction band transition (c); (b), (d) computed normalized degree of optical polarization η (see text) as a function of quasi-momentum $\mathbf{k}$ in the relevant portion of the Brillouin zone for the valence to conduction and core to conduction band transitions, respectively; (e) partial absorption cross-section (σ) obtained through the integration over circular area around $\mathbf{K}_\pm$ points for the left (−) and right (+) circular polarization of the incoming x-ray photons [see also text and illustration of the absorption process in the bottom of panel (e)].

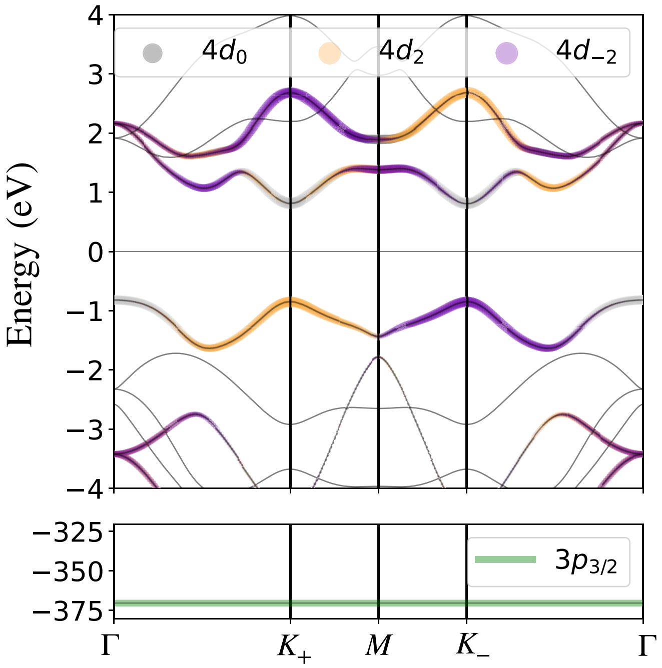

FIG. 5. Band structure of MoS_2 monolayer, where we highlight the projection of the Kohn-Sham wave function onto the $4d_m$ $m = \{0, \pm 2\}$ and $3p_{j=3/2}$ orbitals of the molybdenum atom.

(Fig. 4). The dominant contribution from the corresponding valley ($\mathbf{K}_+$ for right circular polarization and $\mathbf{K}_-$ for the left), however, highlights strong selectivity (see Fig. 3).

The calculations, besides confirming the opposite value of η at the $\mathbf{K}_+$, $\mathbf{K}_-$ points for valence band transitions, also reveal that the strong polarization character persists in very large portions of the Brillouin zone, as one moves away from these points; a fact that would not be easily predictable by group theory, but that is in complete analogy to the findings of Cao *et al.* [2] for transitions at the fundamental gap. This is an aspect that is important for soft-x-ray spectroscopy, because it implies that the valley selectivity is not going to be washed out by the relatively larger bandwidth of x-ray pulses. The DFT calculations also underline very different behavior of transitions to the conduction bands, where, besides confirming the zero selectivity at the $\mathbf{K}_\pm$ points, they reveal a very different distribution of η in the two regions surrounding the points. To study the role of the orbital character in the selection rules for the whole Brillouin we performed a projection of the Kohn-Sham wave functions onto the basis of the local orbitals of the molybdenum atom and results are presented in Fig. 5. Qualitatively, instead of almost uniform distribution, which we observed for the core to valence band transition, the η distribution for the core to conduction band transitions shows two types of subvalleys with the opposite signs. The first type comprises the valleys around the $K_\pm$ point, and the second the small triangular valleys in between $K_\pm$ and Γ. The latter corresponds to the local minimum of the conduction band (Fig. 5). The opposite selectivity of the two subvalleys is related to the d orbital character of the conduction bands where d_2 and d_{-2} interchange each other around local and global minima. From Fig. 5 we could also see that for the conduction band in the close vicinity of the $K_\pm$ the d_0 type of orbitals have the most substantial contribution and correlate with the absence of dichroism predicted from group theory. Furthermore, for the valence band, orbital characters $d_{\pm 2}$ are dominant in $K_\pm$ valleys, respectively, which expand almost up to Γ point and lead to the more isotropic distribution of η. In line with the conclusion of the previous section our *ab initio* calculations highlight that the symmetry of the local orbitals involved in the transition lies at the very origin of the valley selectivity.

IV. SOFT-X-RAY CORE-LEVEL SPECTROSCOPY: APPLICATIONS TO "VALLEYTRONICS"

The main result of the previous sections is the valley selectivity of transitions from the metal s and p core levels to the valence bands. To have empty states near the valence band top, the available options are gated devices, typically with a MTDM sandwiched between hBN layers with electrodes at the bottom and the top [29], or optical pumping, as in Refs. [6–8] and possibly p-type doping [30,31]. If we postpone for the time being the discussion on the feasibility of XUV and soft-x-ray transmission measurements in atomically thin samples, then novel diagnostic tools for valleytronics can be envisaged. For example, taking inspiration from the pump-probe transient absorption experiments reported by Chang *et al.* [7] at the W $5p_{3/2}$ edge of multilayer WS_2 samples, consider the pump-probe experiments for the monolayer case schematically displayed in Figs. 6(c) and 6(d). Here we propose to use circularly polarized pump and probe pulses; we argue that a circularly polarized pump pulse should induce a pronounced *circular dichroism* in the pump absorption. If the pump and the probe polarizations are the same [Fig. 6(c)], then the transient absorption of the probe should be observed at very small delay, because the transitions from the core levels access the valley in which a hole population was created by the pump. As the delay of the two pulses increases the transient absorption should be attenuated, with characteristic time τ, given by

$$1/\tau = 1/\tau_{\mathrm{rec}} + 1/\tau_{\mathrm{trans}}, \tag{34}$$

because the hole population is reduced by recombination (rec) and by transfer(trans) of holes to other valleys. If the probe polarization is inverted [Fig. 6(d)], then the probe can now promote core electrons only to the valley opposite to the one populated with holes by the pump: the absorption signal is therefore much smaller than in the previous case at short delay times, and can possibly build up in time, if sufficient transfer to the opposite valley takes place, with characteristic time

$$1/\tau = 1/\tau'_{\mathrm{trans}} \tag{35}$$

(where the prime acknowledges that only transfers to the opposite valley are included, and not, e.g., to the Γ valley). At any delay time, therefore, the absorption of the pump pulse should display circular dichroism and, according to Eqs. (33) and (34), should deliver information on the characteristic decay times of the valence valley polarization.

To consider specifics related to WS_2 monolayer, we performed calculations of the normalized polarization degree for transitions first from the core levels ($5p_{3/2}$ of W) to the uppermost of the valence bands [Fig. 6(a)] and then from

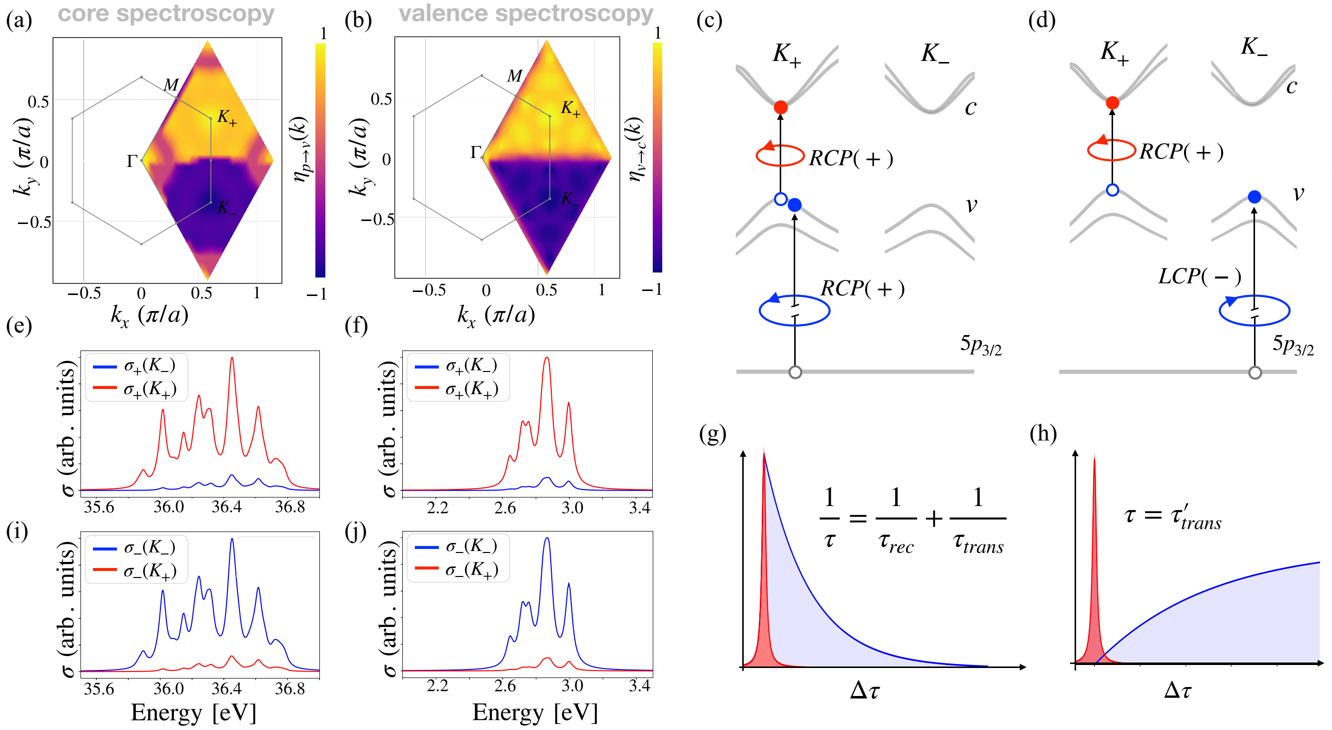

FIG. 6. Valley selectivity of WS_2 and schematic of pump-probe experiment. (a), (b) Normalized degree of optical polarization as a function of quasi-momentum for transitions from W $5p_{3/2}$ levels to the uppermost valence band (a), and from the uppermost valence band to the lowest conduction band (b). (f), (j) [(e), (i)] Partial absorption cross-sections calculated in vicinity of $\mathbf{K}_\pm$ points for the valence to conduction (core to valence) band transitions. (c), (d) Schematic representation of the core to valence and valence to conduction bands transitions for the optical and x-ray photons with the same (c), and opposite (d), circular polarization. The vertical red arrows denote transitions from IR/visible laser pump pulses, the blue arrows transitions from core levels. (g), (h) Schematic figures of the pump pulse (in red) and the transient probe absorption (in blue) as a function of pump-probe delay $\Delta\tau$ for the configuration of polarization presented in panels (c) and (d), respectively. See text for the definition of the various characteristic times τ.

the uppermost of the valence bands to the lowest of the conduction bands [Fig. 6(b)]. As a result, both core and optical transitions show pronounced valley selectivity with the same sign in $\mathbf{K}_+$ and $\mathbf{K}_-$ valleys. The latter means that if circular polarization of the optical and x-ray photons are the same, we can probe information about the single valley; and if, however, they are different, contributions from cross valleys processes will be dominant. In contrast to the previous section, calculations for WS_2 include relativistic effects for core and valence electrons and consequently reproduce spin-orbit splitting of ~8 eV for $5p$ states of tungsten, and ~0.3 eV for the valence d states. The results are presented in Fig. 6 and agrees with the group theoretical predictions. It is also worth noticing that the two valleys are extended through the most part of the Brillouin zone and manifest strong difference in partial absorption. In Figs. 6(a), 6(e), and 6(i) we are showing only characteristic contributions from those $5p_{3/2}$ fourfold degenerate levels that participate in nonzero transitions at the $\mathbf{K}_\pm$ points, contribution from the rest of $5p_{3/2}$ levels favorably support the conclusion in the extended valley region but lead to the divergence of the polarization degree due to the zero denominator. As expected from the group theoretical analysis the core to the lowest conduction band transitions are not valley selective at $\mathbf{K}_\pm$, but have certain selectivity for the small parts of the Brillouin zone (see also Appendix C). Following the approach stated in the previous section we obtained partial absorption cross-sections for the both types of transitions which confirms strong dichroism through the entire energy range of the highest (lowest) valence (conduction) bands.

It is generally presumed that intervalley transfer occurs for excitons, via exciton-exciton or exciton-phonon scattering, with much higher probability than for single carriers (electrons or holes) as the latter case implies either a spin flip or a sizable energy difference [1]. Nonetheless, it is worthwhile to notice that the core electron circular polarization transitions are strictly a probe of the hole population, unlike, e.g., photoluminescence. In special cases, such as the presence of nonradiative recombination or trapping centers for either carrier, the distinction may become relevant.

The actual feasibility of core-level absorption spectroscopy on single layer samples deserves discussion, in particular in the pump-probe mode as discussed above, although recent XAS measurements of monolayer MoS_2 at various core thresholds, performed by electron yield at the SSRL synchrotron in Stanford, are encouraging [32].

With respect to the results reported in Ref. [7], there is, on the one hand, the reduction from several tens of layers to one, and the requirement of circularly polarized photons, on the other hand. To the former challenge, the possible strategies could involve the growth of samples in which single layers are stacked with a hBN spacer in between; and also the selection of a more intense source. By replacing the HHG source used in Ref. [7] with a free-electron laser such as the FERMI facility [10], the intensity increases by about 2 to 3 orders of magnitude; and one can ripe the additional benefit of satisfying the requirement of circularly polarized photons.

Another technique to explore the intervalley relaxation of carriers is time-resolved Kerr rotation (TRKR) [33,34] which has been used in samples where tuning the Fermi level by the gate potential produces, independent of optical pumping, an equilibrium population of electrons or one of holes. In presence of these so-called *resident* carriers, optical pumping with circularly polarized photons near the band gap produces, in one of the valleys, a rapidly decaying population of charged excitons, or trions, which results in an upset of the balance in the population of the two valleys. The imbalance corresponds to a nonzero value of the orbital angular momentum. The exact role of the trions decay and the role of non radiative traps due to impurities is not completely clear [34]. In any event, the measurement of the decay time of the Kerr rotation allows access to the decay times of the difference in valley population of electrons in n-type samples and of holes in p-type samples. The latter case is especially interesting as decay times as long as several μs are observed. In these samples, generation of the holes imbalance between the valleys could be produced by transitions from the core levels with circularly polarized x-ray photons to the valence bands, without intermediate stages in which excitons or trions are present. The core hole would be very rapidly filled by Auger processes or by x-ray fluorescence from electron levels from the whole valence bands; such core hole annihilation should not involve any valley selectivity and should therefore not influence the Kerr rotation signal. This would therefore simplify the understanding of the imbalance relaxation paths and of the corresponding timescales.

V. CONCLUSIONS

In summary the conclusions of the present analysis of the selection rules for transitions in core-level spectroscopy in MTMD are that:

(1) The valley selectivity of circular polarization transitions to the conduction band minima is not to be expected for s-, p-, or d-like metal core levels, as shown by group-theoretical arguments and by *ab initio* calculations, in contrast to the well-known top of the valence to conduction valleytronic selectivity.

(2) Valley selectivity is, however, expected for transitions from s- and p-like core levels (but not for d-like levels) to valence states (in contrast to the well known top of the valence-to-conduction selectivity, valleytronics), and conversely for x-ray emission. This conclusion assumes of course that the valence bands are not completely full, as can be obtained in a static way by electrostatic biasing, or in a static or time-dependent way by optical pumping.

(3) We argued that these selection rules open the way to a new tool for the study and time resolved monitoring of valleytronics in 2D-TMD, and a specific example was discussed.

The potential applications, however, are not limited to the idea of using an x-ray pulse as a probe. In fact, another possibility to profit from derived selection rules is to use the core-to-valence transition under circularly polarized light to create an imbalanced population in the two valleys for the initially hole-doped TMD sample. That would allow more direct access to dynamics of the hole/electron carriers without creating multiparticle excitations (e.g., excitonis, trions), which accompany transitions in the optical region.

Before further considering possible experimental implications of the results derived here for core-level transitions, the following points should be taken into account:

(1) Feasibility of specific experiments, depending on the actual cross sections, considering the extremely diluted character of monolayer samples.

(2) Excitonic effects. The valence to conduction spectroscopy is strongly affected by exciton effects [1], as expected from considerations on screening of the electron-hole interaction in low-dimensional systems. The same arguments should apply to electron-core hole interactions, and core excitons can be expected to modify the transition energies and intensities, but not necessarily the symmetry considerations discussed here. In general, if a pair of bands are connected by an allowed dipole transition, then so is the corresponding ground exciton state.

(3) The just mentioned dipole approximation, i.e., the assumption that the photon momentum is negligible in comparison to the size of the Brillouin zone. This is reasonable for the shallowest core levels, like the M edges of Mo or the N edges of W, but certainly not for the deeper ones.

(4) The lifetime broadening of core levels (especially the deeper ones) is a limitation of the achievable energy resolution. In some cases it can prevent a clear distinction of transitions to the $\mathbf{K}_{\pm}$ valleys from nearby secondary band extrema, requiring a specific discussion of each compound.

Finally, we considered a material with close structural symmetry but without strong spin-orbit coupling such as hBN. We confirmed valley selectivity for excitations in the optical region and derived corresponding selection rules. However, there are very few dipole allowed transitions from core levels to the lowest conduction and valence band and in total they do not show the valley selectivity.

ACKNOWLEDGMENTS

We thank Kin-Fai Mak, Jie Shan, and Claudio Masciovecchio for interesting discussions. This work was supported by the Cluster of Excellence “CUI Advanced Imaging of Matter”- EXC 2056 - Project ID 390715994 and SFB-925 “Light induced dynamics and control of correlated quantum systems” - Project 170620586 of the Deutsche Forschungsgemeinschaft (DFG), and by the project Grupos Consolidados of the Basque University System (IT1249-19). A.G. thank Dong Eon Kim and was supported by a National Research Foundation of Korea grant funded by the Ministry of Science and ICT, Grant No. 2016K1A4A4A01922028.

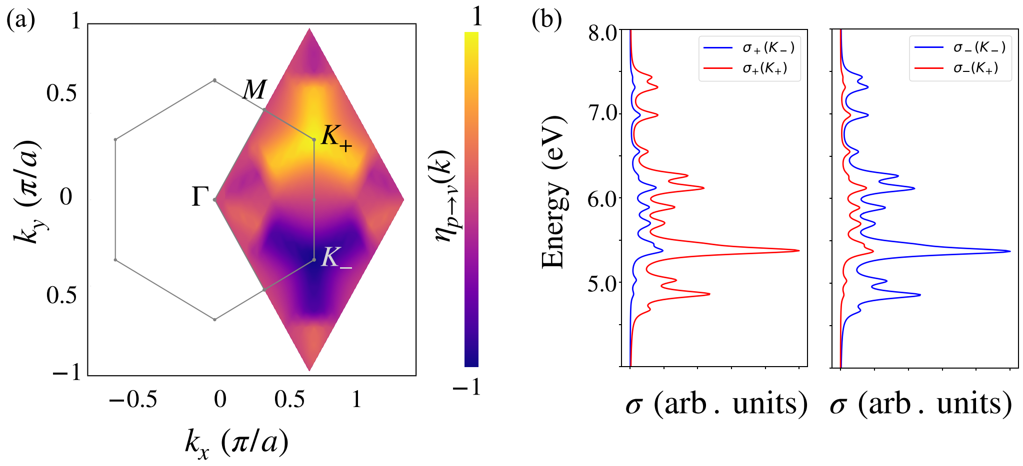

FIG. 7. (a) Computed normalized degree of optical polarization η (see text) for transitions from the hBN highest valence band the lowest conduction band, as a function of quasi-momentum $\mathbf{k}$ in the relevant portion of the Brillouin zone. (b) Partial absorption cross-section calculated for the circular area around $\mathbf{K}_\pm$ points for left (−) and right (+) circular polarization of the incoming photons (see also Sec. III).

APPENDIX A: VALLEY SELECTIVITY WITHOUT SPIN-ORBIT COUPLING: hBN

The purpose of this Appendix is to briefly consider the valley-selective effects in monolayer hexagonal boron nitride, hBN, with a simple extension of the discussion given in Sec. II A. In fact, the lattice symmetry for a monolayer of hBN is identical to that of 2D-TMD, with D_{3h} as point group and C_{3h} as the wave vector group at the $\mathbf{K}_\pm$ points [35]. According to the prevailing results of DFT theoretical work, the valence band top of monolayer hBN is located at the $\mathbf{K}_\pm$ points; whether the conduction band minimum is at Γ or at $\mathbf{K}_\pm$ is a very close call [36–39] and the computed gap is extremely sensitive to the chosen functional and to details of the numerical procedure [40]. Nonetheless, even if the lowest gap is indirect, optical properties are very likely dominated by the larger oscillator strength of the direct transition, and experimental evidence [41] points in this direction. We are going to consider transitions at these direct gaps to provide an example of nonvanishing valley selectivity in a system in which, with good approximation, the spin-orbit interaction can be neglected (see Fig. 7).

The group theoretical analysis can follow the pattern of Eq. (5) and following of Sec. II A, the only difference being the orbital character of the Wannier-like functions for hBN. According to the band structure calculations, see for example Ref. [36], the dominant character of the conduction band minima is derived from the B $2p_z$ states, whereas the valence band top is ascribed to $2p_z$ orbitals of the N atoms. Given the low atomic number of these elements, spin-orbit interactions are negligible. Starting with the conduction band minimum at $\mathbf{K}_+$, we observe that the $2p_z$ orbitals are invariant for all proper rotations about the z axis ($m = 0$), but are odd under all operations reversing the z axis directions, i.e., σ_z, $S_3^\pm$. A look at the character table of C_{3h} associates this behavior to Γ_4 representation. The symmetry character of the exponential Bloch factor for the metal sites is identical to the MTMD case and belongs to the Γ_3 irreducible representation. Finally, the spin wave function belongs to the reduction of the $D_{1/2}^+$ representation that gives $\Gamma_7 + \Gamma_8$. Putting all together, the conduction band minimum at $\mathbf{K}_+$ for the two spin directions is associated to

$$\Gamma_3 \otimes \Gamma_4 \otimes \Gamma_7 = \Gamma_8, \quad \Gamma_3 \otimes \Gamma_4 \otimes \Gamma_8 = \Gamma_{11}. \tag{A1}$$

Consider now the top valence bands, corresponding to similar $2p_z$ orbitals of N, centered however on the "empty" vertices of the lattice sketched in Fig. 2. These sites can be indexed in analogy to Eq. (6) as

$$\mathbf{R}^N_{j_1,j_2} = j_1\mathbf{a_1} + j_2\mathbf{a_2} + \delta_3 + \delta_2. \tag{A2}$$

Note that with this indexing, since $\mathbf{K}_+ \cdot \delta_2 = 0$, both j_1, j_2 -indexed anion and cation sites belong to the same wavefront and have a common phase,

$$\exp\left[i\mathbf{K}_+ \cdot \mathbf{R}^{B,N}_{j_1,j_2}\right] = \exp\left[i(2j_1 + j_2 - 1)\frac{2\pi}{3}\right]. \tag{A3}$$

Repeating the procedure outlined in Appendix B, and noting that $C_3^- \delta_2 = \delta_3$ we find that after a C_3^+ rotation, the phase factor of the N sites becomes

$$\exp\left[i(-j_1 - 2j_2)\frac{2\pi}{3}\right] \equiv \exp\left[i(2j_1 + j_2)\frac{2\pi}{3}\right], \tag{A4}$$

and, in general, $C_3^\pm$, $S_3^\pm$ produce a factor $e^{\pm(i2\pi/3)}$, which allows us to associate the Bloch factor at the N sites to the Γ_2 representation.

The valence bands analogous of Eq. (A1) becomes then

$$\Gamma_2 \otimes \Gamma_4 \otimes \Gamma_7 = \Gamma_{12}, \quad \Gamma_2 \otimes \Gamma_4 \otimes \Gamma_8 = \Gamma_7. \tag{A5}$$

It is readily seen that if we now consider the same bands at $\mathbf{K}_-$ we must interchange Γ_2 and Γ_3 in Eqs. (A1) and (A5), obtaining the band schematic diagram in Fig. 8. The usual procedure allows us to derive the selection rules for circularly polarized light at $\mathbf{K}_+$:

Initial	Final	Polarization
Γ_{12}	Γ_8	−
Γ_7	Γ_{11}	−

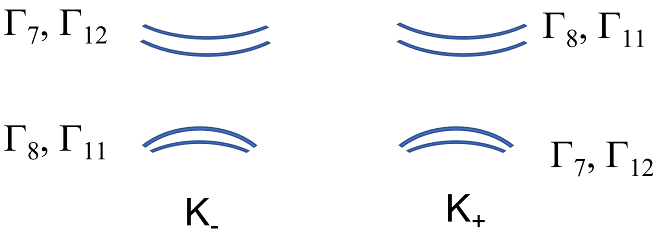

FIG. 8. Schematics of the valence and conduction band edges and their symmetry labels for hBN at the $\mathbf{K}_\pm$ points.

at $\mathbf{K}_-$:

Initial	Final	Polarization
Γ_{11}	Γ_7	+
Γ_8	Γ_{12}	+

showing as valley selectivity effect at the $\mathbf{K}_\pm$ valleys of hBN. Our numerical calculations (Fig. 7) confirm such analysis; however, they also suggest that the valley are smaller then in case of MTMD and elongate toward the Γ point. In considering the transitions from the 1s core levels, however, we find no valley selective circular dichroism probing the highest valence and the lowest conduction bands. This is however not attributable to the negligible spin-orbit interaction, but rather to $2p_z, m = 0$ character of both band edges, resulting in forbidden transitions for circular polarization.

APPENDIX B: SYMMETRY CHARACTER OF THE SPACE PART OF THE BLOCH FUNCTIONS AT $\mathbf{K}_+$

For completeness, we enumerate the steps leading to the conclusion that the space part of the Bloch function (i.e., the part that does not include spin variables) at $\mathbf{K}_+$ transforms as the Γ_3 representation of C_{3h}. The first observation is that the σ_h leaves all factors unchanged, because atomic position vectors lie in the plane, $\Psi_{2,0} \sim (3z^2 - r^2)$ is even and the spin is a pseudovector. Consider now the counterclockwise rotation by $2\pi/3, C_3^+$. To determine its effect on the spatial part of the wave function, i.e., on

$$\sum_{j_1,j_2} e^{i\mathbf{K}_+\cdot\mathbf{R}_{j_1,j_2}}\,\Phi_{2,0}\big(\mathbf{r}-\mathbf{R}_{j_1,j_2}\big), \tag{B1}$$

following Eq. (8) we have to evaluate

$$\sum_{j_1,j_2} e^{i\mathbf{K}_+\cdot\mathbf{R}_{j_1,j_2}}\,\Phi_{2,0}\big(C_3^-(\mathbf{r})-\mathbf{R}_{j_1,j_2}\big). \tag{B2}$$

This can be done by noticing that the sum is unchanged if each $\mathbf{R}_{j_1,j_2}$ is replaced by $C_3^-(\mathbf{R}_{j_1,j_2})$, i.e.,

$$\begin{aligned}&\sum_{j_1,j_2} e^{i\mathbf{K}_+\cdot\mathbf{R}_{j_1,j_2}}\,\Phi_{2,0}\big(C_3^-(\mathbf{r})-\mathbf{R}_{j_1,j_2}\big)\\ &\quad=\sum_{j_1,j_2} e^{i\mathbf{K}_+\cdot C_3^-(\mathbf{R}_{j_1,j_2})}\,\Phi_{2,0}\big[C_3^-\big(\mathbf{r}-\mathbf{R}_{j_1,j_2}\big)\big].\end{aligned} \tag{B3}$$

This is because, when j_1, j_2 run over all integers, both sums on the right- and on the left-hand side run once over each and every metal site. To make further progress, we determine the lines of constant phase of the unrotated Bloch wave [the Bloch wavefronts, shown as dotted lines in Fig. 2, the integer near the top of each line being $(2j_1 + j_2 \bmod 3)$]; the phase factor being given by

$$e^{i\mathbf{K}_+\cdot(j_1\mathbf{a_1}+j_2\mathbf{a_2}+\delta_3)} = e^{i(2j_1+j_2-1)\frac{2\pi}{3}}. \tag{B4}$$

To see the effect of the C_3^- rotation, we notice that its effect is to transport the atom located at $j_1\mathbf{a_1} + j_2\mathbf{a_2} + \delta_3$ to the new location $-(j_1 + j_2)\mathbf{a_1} + j_1\mathbf{a_2} + \delta_\mathbf{1}$. This is readily seen by inspection of Fig. 2, because

$$C_3^-\mathbf{a_1} = \mathbf{a_2} - \mathbf{a_1}, \quad C_3^-\mathbf{a_2} = -\mathbf{a_1}, \quad C_3^-\delta_3 = \delta_\mathbf{1}. \tag{B5}$$

The phase factor associated to the j_1, j_2 term after the rotation becomes

$$e^{i(-j_1-2j_2+1)\frac{2\pi}{3}} \equiv e^{i(2j_1+j_2+1)\frac{2\pi}{3}}, \tag{B6}$$

where the right-hand side results from inserting factors $e^{i3j_i\frac{2\pi}{3}} = 1, i = 1, 2$; comparing to Eq. (12) it is immediately apparent that the action of C_3^+ multiplies each addendum of the Bloch sum by $e^{(i4\pi/3)} \equiv e^{(-i2\pi/3)}$, and likewise in general the elements $C_3^\pm, S_3^\pm$ produce a factor $e^{\mp(i2\pi/3)}$.

Now a simple look at the character table of C_{3h} [15] reveals that these complex factors reproduce exactly the characters of the Γ_3 representation.

The $m = 0$ d-like Wannier function, however, is unaffected by all rotations about the z axis, and it does not affect the overall symmetry of the Bloch function.

APPENDIX C: CORRESPONDENCE BETWEEN SPIN-ORBIT PARTNERS AND IRREDUCIBLE REPRESENTATIONS

The purpose of this Appendix is to deepen the symmetry assignments of the electronic states at $\mathbf{K}_\pm$; for example, it was established, Eqs. (23) and (24), that the doublet of $p_{1/2}$ states with $j_z = \pm 1/2$ belong to the Γ_8 and Γ_{11} representations at $\mathbf{K}_+$; which one corresponds to the $j_z = +1/2$ state? This should allow us to identify the wave functions for a specific representation and to obtain a direct, intuitive picture of the optical selection rules.

The procedure to associate a specific wave function to an irreducible representation, in the somewhat subtle case of a double group, can be derived from Ref. [44].

Let us start from the simple case of the conduction band, where we can basically ignore the spin-orbit interaction. Going back to Eq. (5) and considering one addendum of the Bloch sum, we can write the wave function for spin-up and -down as

$$e^{i\mathbf{K}_+\cdot\mathbf{R}}\,\Phi_{2,0}(\mathbf{r}-\mathbf{R})\begin{pmatrix}1\\0\end{pmatrix}, \tag{C1}$$

$$e^{i\mathbf{K}_+\cdot\mathbf{R}}\,\Phi_{2,0}(\mathbf{r}-\mathbf{R})\begin{pmatrix}0\\1\end{pmatrix}. \tag{C2}$$

There are therefore three parts of the wave function: Bloch sum, a spherical harmonic type orbital, and a spinor. When we act with a C_{3h} operation on it, the wave function is multiplied by a factor that is the product of factors related to the

Bloch exponential, to the orbital and to the spinor. Evaluating this product gives us the character of the operation in the corresponding irreducible representation, and comparing to the character table we can identify the symmetry type of the wave function. The fact that all representations are one-dimensional is of course making this particularly simple. Let us start with the spin-up case and with C_3^+. Looking back to Appendix B, we know already that the Bloch term contributes a factor $e^{-i2\pi/3}$, and the $m = 0$ function a factor 1. The spinors transform according to the $D^+_{1/2}$ representation of $O(3)$, and following Eqs. (3.10)–(3.16) of KDWS, a rotation by an angle α about the z axis corresponds to the matrix

$$D^+_{1/2}(\alpha) = \begin{bmatrix} e^{i\alpha/2} & 0 \\ 0 & e^{-i\alpha/2} \end{bmatrix}. \tag{C3}$$

Therefore, for a $-2\pi/3$ rotation, there is a factor $e^{-i\pi/3}$ for the spin-up case, $e^{i\pi/3}$ for the spin down. Putting it all together, for C_3^+, we get an overall factor -1 for spin up, and $e^{-i\pi/3}$ for spin down. Taking a look at the character table (Table 57 on page 59 of KDWS) this is already sufficient to establish that spin up is Γ_{12} and spin down is Γ_{10}, as Eq. (10) has already restricted the selection to these two representations. For future reference and to appreciate the care needed for the double groups in the general case, it is instructive to obtain the same result again, but this time choosing the σ_h operation. Since Eq. (8), or the equivalent Eqs. (3-10) and (3-11) of KDWS, lead us to apply the *inverse* of σ_h, we must avoid the pitfall of identifying σ_h as its own inverse: in fact the inverse of σ_h is $\overline{\sigma_h}$, which is σ_h plus a 2π rotation (that for a spinor does not coincide with the identity E, because it changes all signs). In fact [43],

$$\sigma_h\overline{\sigma_h} = E, \quad \sigma_h\sigma_h = \overline{E}. \tag{C4}$$

So we know that the effect of σ_h on the Bloch factor and on the $m = 0$ orbital is a factor of 1, to find the action on the spinors we must remember that $\sigma_h = C_2\hat{I}$, a rotation by π times the space inversion. We therefore obtain

$$D^+_{1/2}(\overline{\sigma_h}) = -D^+_{1/2}(\sigma_h) = \begin{bmatrix} -e^{i\pi/2} & 0 \\ 0 & -e^{-i\pi/2} \end{bmatrix}, \tag{C5}$$

where we used the fact that $D^+_{1/2}$ is even under the inversion, and therefore the action of σ_h is equivalent to that of C_2. We therefore conclude that the effect of σ_h for the spin-up state is to multiply it by a factor $-i$, and for the spin-down by i, and a look at the character table confirms the Γ_{12} assignment for spin up, Γ_{10} for spin down. At $\mathbf{K}_-$ the states transforming as Γ_9 and Γ_{11} correspond, respectively, to spin up and spin down as they are identifiable as the time-reversal partners of, respectively, Γ_{10} and Γ_{12}, as already pointed out in the discussion following Eq. (11).

Following the reasoning already adopted at the beginning of Sec. II B, the same assignments are valid also for s-like core levels.

Next we consider the top valence bands. They are unique in their symmetry properties, because as described in Sec. II A, the Bloch factor for $\mathbf{K}_+$ and the $m = 2$ d orbital combine to form a C_{3h} invariant function, and the same happens at $\mathbf{K}_-$ with the $m = -2$ orbital. Therefore, only the behavior of the up and down spinors characterizes the symmetry behavior of the top valence bands, and on the basis of Eq. (42) we can assign Γ_8 to spin up and Γ_7 to spin down. Again the time reversal invariance imposes $E(\mathbf{K}_+, \Gamma_8) = E(\mathbf{K}_-, \Gamma_7)$.

Let us now consider the $p_{1/2}$ levels. The corresponding Bloch functions at $\mathbf{K}_+$ can be written, in spinor notation, as

$$\sum_{j_1,j_2} e^{i\mathbf{K}_+\cdot\mathbf{R}_{j_1,j_2}}\Phi_{1/2,j_z}\big(\mathbf{r} - \mathbf{R}_{j_1,j_2}\big), \tag{C6}$$

where, for $j_z = +1/2$

$$\Phi_{1/2,1/2} = \begin{pmatrix} -\sqrt{1/3}z \\ \sqrt{2/3}(x+iy) \end{pmatrix}, \tag{C7}$$

and, for $j_z = -1/2$,

$$\Phi_{1/2,-1/2} = \begin{pmatrix} \sqrt{2/3}(x-iy) \\ -\sqrt{1/3}z \end{pmatrix}. \tag{C8}$$

To compute the character of an operation $\hat{C}$, following the usual procedure, we must evaluate

$$\sum_{j_1,j_2} e^{i\mathbf{K}_+\cdot\hat{C}^{-1}\mathbf{R}_{j_1,j_2}} D^-_{1/2}(\hat{C}^{-1})\Phi_{1/2,j_z}\big(\hat{C}^{-1}\big(\mathbf{r} - \mathbf{R}_{j_1,j_2}\big)\big). \tag{C9}$$

The effect on the exponential Bloch factor can be evaluated as in the previous sections, and for the spinor we apply the procedure described by KDWS on p. 10 ff., Eqs. (3-13)–(3-16). For example, for the C_3^+ operation, the exponential acquires a factor $e^{-i2\pi/3}$, for the D matrix we can use Eq. (C3) (the ± parity sign intervening for improper rotations only)

$$D^-_{1/2}\big(C_3^{-1}\big) = \begin{bmatrix} e^{-i\pi/3} & 0 \\ 0 & e^{i\pi/3} \end{bmatrix}, \tag{C10}$$

and for the spinor component we simply apply $C_3^-(z) = z$, $C_3^-(x \pm iy) = e^{i\mp 2\pi/3}(x \pm iy)$, to obtain

$$\begin{aligned} C_3^+ \sum_{j_1,j_2} e^{i\mathbf{K}_+\cdot\mathbf{R}_{j_1,j_2}} &\begin{pmatrix} -\sqrt{1/3}z \\ \sqrt{2/3}(x+iy) \end{pmatrix} \\ &= e^{-i2\pi/3} \sum_{j_1,j_2} e^{i\mathbf{K}_+\cdot\mathbf{R}_{j_1,j_2}} \begin{pmatrix} -e^{-i\pi/3}\sqrt{1/3}z \\ e^{i\pi/3}\sqrt{2/3}e^{-i2\pi/3}(x+iy) \end{pmatrix}. \end{aligned} \tag{C11}$$

Therefore, the 1/2, 1/2 partner of the $p_{1/2}$ doublet is multiplied by -1 when acted upon by C_3^+, which associates it to the Γ_{11} representation [see Eq. (23)], while, necessarily, the 1/2, −1/2 partner belongs to Γ_8.

The assignment at $\mathbf{K}_-$ can be inferred by time reversal symmetry, with 1/2, 1/2 belonging to Γ_7, and 1/2, −1/2 belonging to Γ_{12}.

A similar treatment yields the assignments for the four irreducible representations for the $p_{3/2}$ quartet. The four Wannier

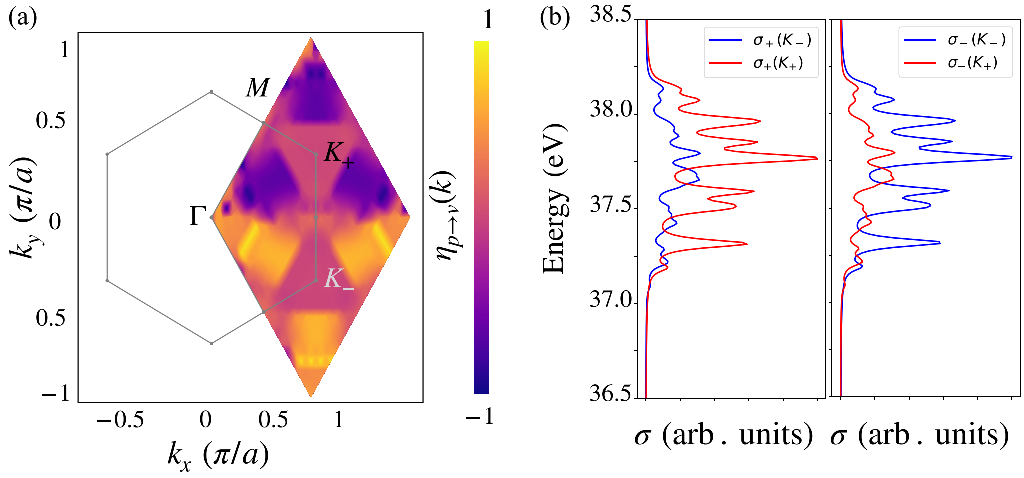

FIG. 9. Computed normalized degree of optical polarization η for transitions from the fourfold degenerate $5_{p_{3/2}}$ levels of tungsten in monolayer WS_2 to the lowest conduction band, as a function of quasi-momentum **k** in the relevant portion of the Brillouin zone (a). Partial absorption cross-section calculated for the circular area around $\mathbf{K}_\pm$ points for left (−) and right (+) circular polarization polarization of the incoming photons (see also Sec. III).

functions can be expressed in spinor notation as

$$\Phi_{3/2,j_z=3/2} = \begin{pmatrix} (x+iy) \\ 0 \end{pmatrix}, \tag{C12}$$

$$\Phi_{3/2,j_z=1/2} = \begin{pmatrix} \sqrt{2/3}z \\ \sqrt{1/3}(x+iy) \end{pmatrix}, \tag{C13}$$

$$\Phi_{3/2,j_z=-1/2} = \begin{pmatrix} \sqrt{1/3}(x-iy) \\ \sqrt{2/3}z \end{pmatrix}, \tag{C14}$$

$$\Phi_{3/2,j_z=-3/2} = \begin{pmatrix} 0 \\ (x-iy) \end{pmatrix}, \tag{C15}$$

and repeating the previous procedure we get at $\mathbf{K}_+$:

$$\begin{aligned} &\Phi_{3/2,j_z=3/2} \longrightarrow \Gamma_9, \quad \Phi_{3/2,j_z=1/2} \longrightarrow \Gamma_{11}, \\ &\Phi_{3/2,j_z=-1/2} \longrightarrow \Gamma_8, \quad \Phi_{3/2,j_z=-3/2} \longrightarrow \Gamma_7, \end{aligned} \tag{C16}$$

and by time-reversal at $\mathbf{K}_-$:

$$\begin{aligned} &\Phi_{3/2,j_z=3/2} \longrightarrow \Gamma_8, \quad \Phi_{3/2,j_z=1/2} \longrightarrow \Gamma_7, \\ &\Phi_{3/2,j_z=-1/2} \longrightarrow \Gamma_{12}, \quad \Phi_{3/2,j_z=-3/2} \longrightarrow \Gamma_{10}. \end{aligned} \tag{C17}$$

APPENDIX D: WS_2: CORE-TO-CONDUCTION BAND TRANSITIONS

For the experiment described in Sec. IV, it is essential to have valley selectivity for the transitions from and to the top of the valence band. However, the valley selectivity is not expected for transitions from p core levels to the conduction band minima at the $\mathbf{K}_\pm$ points, according to the findings of the group theoretical analysis of Sec. II. It is interesting to explore the first principle calculations for the WS_2 monolayer in some detail (see Fig. 9). In fact, transitions from each individual W $5p_{3/2,m_j}$ level are valley selective, but transitions with positive and negative m_j have an equal and opposite valley sensitivity and cancel each other completely around the $\mathbf{K}_\pm$ points. Similar to what is found also in MoS_2, there are small secondary valleys in between $\mathbf{\Gamma}$ and $\mathbf{K}_\pm$ points which show a partial degree of dichroism [see Fig. 9(b)]. The latter could be relevant for the future studies involving relaxation and intervalley scattering.

APPENDIX E: X-RAY EDGES FOR Mo AND W

We reproduce here the atomic binding energies of some of the core levels of Mo and W, for convenience of the reader (Table I).

TABLE I. Atomic binding energies of Mo and W core levels in eV; hard x-ray levels >3 keV are omitted (from Ref. [42]).

Level	$L_1(2s_{1/2})$	$M_1(3s_{1/2})$	$N_1(4s_{1/2})$	$O_1(5s_{1/2})$	$M_2(3p_{1/2})$	$M_3(3p_{3/2})$	$M_4(3d_{3/2})$
Mo	2866	506.3	63.2		411.6	394.0	231.1
W		2820	594.1	75.6	2575	2281	1872
Level	$M_5(3d_{5/2})$	$N_2(4p_{1/2})$	$N_3(4p_{3/2})$	$N_4(4d_{3/2})$	$N_5(4d_{5/2})$	$O_2(5p_{1/2})$	$O_3(5p_{3/2})$
Mo	227.9	37.6	35.5				
W	1809	490.4	423.6	255.9	243.5	45.3	36.8

[1] G. Wang, A. Chernikov, M. Glazov, T. F. Heinz, X. Marie, T. Armand, and B. Urbaszek, Excitons in atomically thin transition metal dichalcogenides, Rev. Mod. Phys. **90**, 021001 (2018).

[2] T. Cao, G. Wang, W. Han, H. Ye, C. Zhu, J. Shi, Q. Niu, P. Tan, E. Wang, B. Liu, and J. Feng, Valley-selective circular dichroism of monolayer molybdenum disulphide, Nat. Commun. **3**, 887 (2012).

[3] D. Xiao, G.-B. Liu, W. Feng, X. Xu, and W. Yao, Coupled Spin and Valley Physics in Monolayers of MoS_2 and Other Group-VI Dichalcogenides, Phys. Rev. Lett. **108**, 196802 (2012).

[4] S. A. Vitale, D. Nezich, J. O. Varghese, P. Kim, N. Gedik, P. Jarrillo-Herrero, D. Xiao, and M. Rothschild, Valleytronics: Opportunities, challenges and paths forward, Small **14**, 1801483 (2018).

[5] see for example E. Cappelluti, R. Roldán, J. A. Silva-Guillén, P. Ordejón, and F. Guinea, Tight-binding model and direct-gap/indirect-gap transition in single-layer and multilayer MoS_2, Phys. Rev. B **88**, 075409 (2013).

[6] A. R. Attar, H-T. Chang, A. Britz, X. Zhang, M.-F. Lin, A. Krishnamoorthy, T. Linker, D. Fritz, D. M. Neumark, R. K. Kalia *et al.*, Simultaneous observation of carrier-specific redistribution and coherent lattice dynamics in 2H-$MoTe_2$ with femtosecond core-level spectroscopy, ACS Nano **14**, 15829 (2020).

[7] H. T. Chang, A. Guggenmos, C. T. Chen, J. Oh, R. Géneaux, Y.-D. Chuang, A. M. Schwartzberg, S. Aloni, D. M. Neumark, and A. R. Leone, Coupled valence carrier and core-exciton dynamics in WS_2 probed by few-femtosecond extreme ultraviolet transient absorption spectroscopy, Phys. Rev. B **104**, 064309 (2021).

[8] A. Britz, A. R. Attar, X. Zhang, H-T. Chang, C. Nyby, A. Krishnamoorthy, S. H. Park, S. Kwon, M. Kim, D. Nordlund *et al.*, Carrier-specific dynamics in 2H-$MoTe_2$ observed by femtosecond absorption spectroscopy using an x-ray free-electron laser, Struct. Dyn. **8**, 014501 (2021).

[9] Y. Song and H. Dery, Transport Theory of Monolayer Transition Metal Dichalcogenides Through Symmetry, Phys. Rev. Lett. **111**, 026601 (2013); see in particular Supplemental Material.

[10] See for example the relevant parameters for the FERMI free-electron laser facility: https://www.fels-of-europe.eu/fel_facilities/x_ray_facilities/fermi/.

[11] A. Kormányos, G. Burkard, M. Gmitra, J. Fabian, V. Zólyomi, N. D. Drummond, and V. Fal'ko, **kp** theory for two-dimensional transition metal dichalcogenide semiconductors, 2D Mater. **2**, 022001 (2015).

[12] C. Kittel, *Quantum Theory of Solids* (Wiley, New York, 1963), pp. 182–184.

[13] M. Tinkham, *Group Theory and Quantum Mechanics* (McGraw-Hill, New York, 1964).

[14] C. J. Bradley and A. P. Cracknell, *The Mathematical Theory of Symmetry in Solids*, (Clarendon Press, Oxford, 1972).

[15] G. F. Koster, J. O. Dimmock, R. G. Wheeler, and H. Statz, *Properties of the Thirty-two Point Groups* (MIT Press, Cambridge, MA, 1963).

[16] H. Ochoa and R. Roldán, Spin-orbit-mediated spin relaxation in monolayer MoS2, Phys. Rev. B **87**, 245421 (2013).

[17] A. Kormányos, V. Zólyomi, N. D. Drummond, P. Rakyta, G. Burkard, and V. Fal'ko, Monolayer MoS_2: Trigonal warping, the Γ valley, and spin-orbit coupling effects, Phys. Rev. B **88**, 045416 (2013).

[18] The C_{3h} character table is Table 57, p. 59 of Ref. [15].

[19] Table 62 on p. 62 of Ref. [15].

[20] See Chap. 2 and Sec. 3.3 of Chap. 3 of Ref. [15].

[21] See Sec. 4.9 of Ref. [13].

[22] See Table 58 of Ref. [15].

[23] See also Eqs. (4)–(7), p. 64 of Ref. [13].

[24] See Table 57 of Ref. [15].

[25] A. Gulans, S. Kontur, C. Meisenbichler, D. Nabok, P. Pavone, S. Rigamonti, S. Sagmeister, U. Werner, and C. Draxl, Exciting: A full-potential all-electron package implementing density-functional theory and many-body perturbation theory, J. Phys.: Condens. Matter **26**, 363202 (2014).

[26] O. K. Andersen, Linear methods in band theory, Phys. Rev. B **12**3060 (1975).

[27] J. P. Perdew, K. Burke, and M. Ernzerhof, Generalized Gradient Approximation Made Simple, Phys. Rev. Lett. **77**, 3865 (1996)

[28] C. Vorwerk, C. Cocchi, and C. Draxl, Addressing electron-hole correlation in core excitations of solids: An all-electron many-body approach from first principles, Phys. Rev. B **95**, 155121 (2017).

[29] See, e.g., the review by K. F. Mak and J. Shan, Photonics and optoelectronics of 2D semiconductor transition metal dichalcogenides, Nat. Photonics **10**, 216 (2016).

[30] B. Tang, Z. G. Yu, L. Huang, J. Chai, S. L. Wong, J. Deng, W. Yang, H. Gong, S. Wang, K.-W. Ang, Y.-W. Zhang, and D. Chi, Direct *n*- to *p*-type channel conversion in monolayers/few-layer WS_2 field-effect transistors by atomic nitrogen treatment, ACS Nano **12**, 2506 (2018).

[31] Q. Liang, J. Gou, Arramel, Q. Zhang, W. Zhang, and A. T. Shen Wee, Oxygen-induced controllable *p*-type doping in 2D semiconductor transition metal dichalcogenides, Nano Res. **13**, 3439 (2020).

[32] S. Park, A. T. Garcia-Esparza, H. Abroshan, B. Abraham, J. Vinson, A. Gallo, D. Nordlund, J. Park, T. R. Kim, L. Vallez *et al.*, Operando study of thermal oxidation of monolayer MoS_2, Adv. Sci. **8**, 2002768 (2021)

[33] P. Dey, L. Yang, C. Robert, G. Wang, B. Urbaszek, X. Marie and S. A. Crooker, Gate-Controlled Spin-Valley Locking of Resident Carriers in WSe_2 Monolayers, Phys. Rev. Lett. **119**, 137401 (2017).

[34] M. Ersfeld, F. Volmer, L. Rathmann, L. Kotewitz, M. Heithoff, M. Lohmann, B. Yang, K. Watanabe, T. Taniguchi, L. Bartels *et al.*, Unveiling valley lifetimes of free charge carriers in monolayer WSe_2, Nano Lett. **20**, 3147 (2020).

[35] E. Doni and G. Pastori-Parravicini, Energy bands and optical properties of hexagonal boron nitride and graphite, Il Nuovo Cimento B (1965-1970) **64**, 117 (1969).

[36] M. Topsakal, E. Aktürk, and S. Ciraci, First-principles study of two- and one-dimensional honeycomb structures of boron nitride Phys. Rev. B **79**, 115442 (2009).

[37] H. Şahin, S. Cahangirov, M. Tosakal, E. Bekaroglu, E. Aktürk, R. T. Senger, and S. Ciraci, Monolayer honeycomb structures of group-IV elements and III-V binary compounds: First principles calculations, Phys. Rev. B **80**, 155453 (2009).

[38] B. Huang and H. Lee, Defect and impurity properties of hexagonal boron nitride: A first principles calculation, Phys. Rev. B **86**, 245406 (2012).

[39] D.-H. Kim, H.-S. Kim, M. W. Song, S. Lee, and S. Y. Lee, Geometric and electronic structures of monolayer hexagonal boron nitride with multi-vacancy, Nano Converg. **4**, 13 (2017).

[40] N. Berseneva, A. Gulans, A. V. Krasheninnikov, and R. M. Nieminen, Electronic structure of boron nitride sheets doped with carbon from first-principles calculations, Phys. Rev. B **87**, 035404 (2013).

[41] C. Elias, P. Valvin, T. Pelini, A. Summerfield, C. J. Mellor, T. S. Cheng, L. Eaves, C. T. Foxon, P. H. Beton, S. V. Novikov, B. Gil, and G. Cassabois, Direct band-gap crossover in epitaxial monolayer boron nitride, Nat. Commun. **10**, 2639 (2019).

[42] *X-ray Data Booklet*, 3rd ed., edited by A. C. Thompson (Lawrence Berkeley National Laboratory, University of California, Berkeley, CA, 2009), Table 1.1.

[43] See Ref. [15], p. 5.

[44] See Chap. 2 and Sec. 3.3 of Chap. 3 [15].